International Journal of Biological Macromolecules 273 (2024) 133086

Contents lists available at ScienceDirect

International Journal of Biological Macromolecules

journal homepage: www.elsevier.com/locate/ijbiomac

A computational study to assess the pathogenicity of single or combinations of missense variants on respiratory complex I

Laura Rigobello [a], Francesca Lugli [b,*], Leonardo Caporali [c], Alessio Bartocci [d,e], Jacopo Fadanni [b], Francesco Zerbetto [b], Luisa Iommarini [a], Valerio Carelli [c,f], Anna Maria Ghelli [a,c], Francesco Musiani [a,*]

[a] Department of Pharmacy and Biotechnology, University of Bologna, Bologna I-40127, Italy
[b] Department of Chemistry "Giacomo Ciamician", University of Bologna, Bologna I-40126, Italy
[c] IRCCS Istituto delle Scienze Neurologiche di Bologna, Programma di Neurogenetica, Bologna I-40124, Italy
[d] Department of Physics, University of Trento, Trento I-38123, Italy
[e] INFN-TIFPA, Trento Institute for Fundamental Physics and Applications, Trento I-38123, Italy
[f] Department of Biomedical and Neuromotor Sciences, University of Bologna, Bologna I-40123, Italy

ARTICLE INFO

Keywords:
Mitochondria
Molecular dynamics simulations
Leber's hereditary optic neuropathy
Pathological variants

ABSTRACT

Variants found in the respiratory complex I (CI) subunit genes encoded by mitochondrial DNA can cause severe genetic diseases. However, it is difficult to establish *a priori* whether a single or a combination of CI variants may impact oxidative phosphorylation. Here we propose a computational approach based on coarse-grained molecular dynamics simulations aimed at investigating new CI variants. One of the primary CI variants associated with the Leber hereditary optic neuropathy (m.14484T>C/*MT-ND6*) was used as a test case and was investigated alone or in combination with two additional rare CI variants whose role remains uncertain. We found that the primary variant positioned in the E-channel region, which is fundamental for CI function, stiffens the enzyme dynamics. Moreover, a new mechanism for the transition between π- and α-conformation in the helix carrying the primary variant is proposed. This may have implications for the E-channel opening/closing mechanism. Finally, our findings show that one of the rare variants, located next to the primary one, further worsens the stiffening, while the other rare variant does not affect CI function. This approach may be extended to other variants candidate to exert a pathogenic impact on CI dynamics, or to investigate the interaction of multiple variants.

1. Introduction

Respiratory complex I (CI, EC 1.6.5.3) is the largest enzyme of the mitochondrial respiratory chain [1,2]. In mammals, CI is under a dual genetic control as out of its 44 subunits, 7 (namely ND1–6 and ND4L) are encoded by the multicopy mitochondrial genome (mtDNA), whereas the remaining ones and all the assembly factors needed to its biogenesis are encoded by the nuclear genome (nDNA) [3–5]. Pathogenic variants affecting CI subunits have been described in both nDNA and mtDNA-encoded components. This phenomenon leads to variable phenotypic expression, which ranges from severe and lethal infantile encephalopathy known as Leigh syndrome to adult-onset milder phenotypes such as Leber's hereditary optic neuropathy (LHON). These diseases are all characterized by CI dysfunction, that is the most frequent among metabolic disorders in humans [6]. LHON was the first human disease to be associated with mtDNA pathogenic variants [7] and is characterized by subacute loss of central vision in one eye, followed, usually after 3–6 months, by the involvement of the fellow eye due to retinal ganglion cells degeneration [8]. LHON prevalence is currently estimated one in 25,000–50,000 individuals in European population, thus resulting the most frequent mitochondrial disease [9]. About 90 % of LHON cases are induced by one of three common mtDNA point mutations, namely m.3460G>A/*MT-ND1*, m.11778G>A/*MT-ND4*, and m.14484T>C/*MT-ND6* [10]. The remaining 10 % of patients harbors one or more "rare mutations" in mtDNA [11] or unique combination of missense variants [12]. More recently, recessive variants, yet affecting in most cases CI, have been also found to underlie LHON [12].

The pathogenic variants established as risk factor for LHON are characterized by incomplete penetrance and may need either the combination with further genetic factors, or specific environmental

* Corresponding authors.
E-mail addresses: francesca.lugli6@unibo.it (F. Lugli), francesco.musiani@unibo.it (F. Musiani).

https://doi.org/10.1016/j.ijbiomac.2024.133086
Received 21 March 2024; Received in revised form 7 June 2024; Accepted 9 June 2024
Available online 12 June 2024

exposures, to express the disease. Among the supplementary genetic factors, the most studied is the mtDNA itself, which is characterized by an intrinsic variability and has been selected in population-specific haplotypes by evolutionary pressure [13]. For example, the missense m.14484T>C/*MT-ND6* variant to fully express the pathogenic potential and be associated with LHON needs to arise on a haplogroup J background, since other missense mtDNA variants defining this haplogroup may synergically interact to increase its pathogenic potential [14]. As byproduct of this scenario, the m.14484T>C/*MT-ND6* variant may be also recognized in population genetics surveys, reaching a frequency as high as 1 in 800 individuals in absence of any pathology [15,16]. In the latter case, the m.14484T>C/*MT-ND6* variant is preferentially associated with H or U haplogroups. Conversely, specific combinations in single pedigrees have been shown to increase the disease penetrance up to almost complete penetrance as in the case of a Chinese family presenting the co-existence of the primary m.14484T>C/*MT-ND6* pathogenic variant with the rare m.10680G>A/*MT-ND4L* and a third m.13942A>G/*MT-ND5* variants [17]. Hence, the m.14484T>C/*MT-ND6* variant is a good example of the challenges encountered in attributing a specific pathogenic role to mtDNA variants, as since its initial identification the role played in LHON pathogenesis was ambiguous [18,19]. This ambiguity is mainly generated by its frequency in the general population and its weak evidence of functional impact on CI function.

Overall, the LHON pathogenic variants affecting CI induce an impaired ATP synthesis when driven by CI-linked substrates associated with an increase of reactive oxygen species production that, in turn, enhance the sensitivity of cells to apoptosis [20]. Despite the general biochemical defect induced by LHON pathogenic variants is relatively established, the molecular changes triggered by mutated amino acids on CI mechanism are still unknown. However, thanks to the greatly improved understanding of the mechanistic function of CI, gained mainly after the release of cryo-EM and X-ray crystal structures [1,2,21–26], we can now attempt to better define how mtDNA variants may impinge on CI structure and function, in particular when occurring in specific combinations. The CI structure is commonly divided into three functional modules (Fig. 1): *i*) the NADH oxidation module (N module) that catalyzes the electron transfer through a chain of

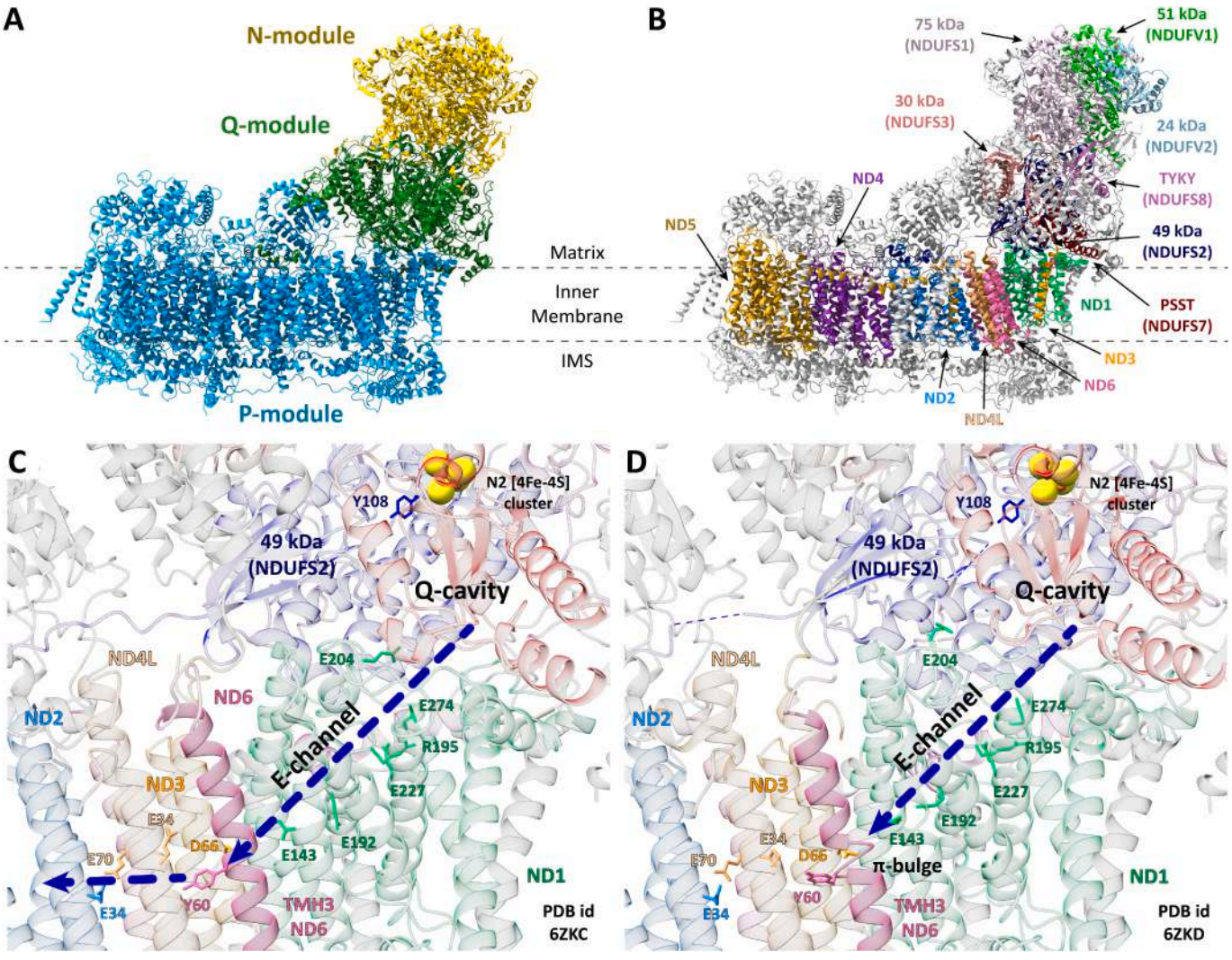

Fig. 1. CI general structure and subunit organization. (**A** and **B**) Cartoon representation of the ovine CI structure (PDB id 6ZKD) across the inner membrane. In panel **A,** the subdivision of the N, Q, and P modules is shown, while in panel **B**, the core subunits are highlighted in different colors (the human gene names are given in brackets), while the supernumerary subunits are in grey. (**C** and **D**) Detail of the Q-cavity and E-channel regions in the closed (**C**, PDB id 6ZKC) and open conformation (**D**, PDB id 6ZKD). The cartoons are colored according to panel **B**. Residues forming the E-channel or important for the CI function are in sticks, while the N2 [4Fe—4S] cluster is shown in spheres colored according to the atom type. ND6 TMH3 and the π-bulge in the open conformation are highlighted, as are the Q-cavity and of the E-channel. The direction of the proton wire is indicated by dashed blue arrows. (For interpretation of the references to colour in this figure legend, the reader is referred to the web version of this article.)

iron-sulfur clusters; *ii*) the ubiquinone reduction module (Q module); and *iii*) the proton translocation module (P module) that induces proton translocation [27]. In particular, the P module is formed by the mtDNA-encoded subunits and is also involved in the formation of the ubiquinone binding site of (called Q-cavity), located at the interface between the Q and P modules (Fig. 1) [1,2,22–26]. Further, the ND1, ND3, ND6 and ND4L subunits form the proximal part of the P module at the interface with the Q module [23–25,28] and together create the E-channel, a region containing several conserved glutamates (Fig. 1) [29,30]. The ND2, ND4 and ND5 subunits form the remaining functional core of the P module. Importantly, in the recently released ovine and *Escherichia coli* structures obtained under a range of redox conditions, including catalytic turnover, CI appears in two distinguishable conformations (open and closed as proposed by Sazanov and coworkers, see ref. [31] for a discussion regarding the different nomenclatures of CI conformations) [21,24,25,31]. Compared to the closed counterpart, in the open conformation the angle formed by the matrix arm (Q plus N modules) with the P module is wider by approximately 7°. Moreover, the open conformation shows some partially disordered regions that are folded in the closed conformation. Finally, some regions change their structure. Specifically, in the open conformation the third trans-membrane helix (TMH3) of ND6 forms a π-bulge (Fig. 1), which breaks the hydrophilic axis in the E-channel region and is proposed to be crucial for CI mechanism, preventing a futile proton leaking towards the Q-cavity [21,28]. Despite the structural and biochemical advances, the mechanism of the proton pumping coupled to the reduction of ubiquinone is still debated [28,32,33]. The complexity of CI structure implies that many amino acids have a crucial role in the conformational changes required for its activity. Therefore, it is conceivable that the combination of amino acid variants, which alone have negligible effect, can affect the activity of CI inducing LHON in some pedigrees. Here, we applied the molecular dynamics (MD) technique with coarse-grained (CG) approach for the study of the effect of mtDNA variants on CI structure. In particular, we investigated the effect of the puzzling primary pathogenic m.14484T>C/*MT-ND6* (p.M64V/ND6) variant, alone or in combination with the rare m.10680G>A/*MT-ND4L* (p.A71T/ND4L) and m.13942A>G/*MT-ND5* (p.T536A/ND5) variants, providing a "proof of principle" that this computational method may be useful for predicting the possible pathogenic effect of specific variant combination. In the present investigation, the term *variant* refers to changes in the nucleotide sequence, while *mutant* refers to the protein models in which one or more amino acids have been changed. Moreover, from now on, the notation reporting the mutation on the translated protein will be used.

Atomistic MD simulations performed on the CI have been used to elucidate aspects of the CI's mechanism of action, such as proton translocation or positioning of water molecules in the so-called hydrophilic axis, or at elucidating the mechanism of inhibition of some known CI's inhibitors [34–55]. Since mammalian CI is a large protein complex, a fully atomistic MD simulation – including a physiological membrane and explicit solvent treatment – implies the use of about 900,000 atoms and a huge computational effort [50,54]. The aims of our approach are *i*) to reduce the computational cost with respect to atomistic simulations using a CG representation and *ii)* to use the minimum number of CI modules necessary to observe dynamic effects attributable to pathogenic mutations. A recently published computational study adopted a similar strategy to study the m.3460G>A/*MT-ND1* LHON primary pathogenic variant through atomistic simulations on an even smaller CI portion [56], highlighting the need to find computationally cheap methods to study CI variants.

2. Results

2.1. Rationale of the computational approach

Here, CG MD simulations were accomplished on the structures comprising the ovine P module and the NDUFS2 subunit (49 kDa subunit in the ovine gene nomenclature, see Table S1 in the Supplementary Information, PDB IDs 6ZKA and 6ZKB) [21]. NDUFS2 structure was partially reconstructed through homology modelling, together with other unsolved regions of the P module (Table S2 and Fig. S1). The resulting model structures were named P+ module to highlight the presence of the NDUFS2 subunit bound to the P module. The MD simulations were initially conducted on the structures of the *wild type* P+ module from *Ovis aries* in both open and closed conformation. The latter simulations were used as control sample, while the simulations of the mutated ovine systems were not performed because some of the residues involved in the studied variants are not conserved in *O. aries*. We then performed a larger set of simulations on homology models of the human *wild type* and mutated P+ modules in both open and closed conformation. Homology models were used instead of the available human structures because of *i*) the lower resolution of the human than the ovine structures and *ii*) the high sequence identity between human and ovine sequences (Table S3). Moreover, the experimental human CI structures were obtained in only one conformation (namely, the open one). Subsequently to the modelling procedure, each system was inserted in a double layer membrane resembling the human inner mitochondrial membrane and solvated in a solution at physiological ionic strength (see Methods section for details).

Regarding the reduction of the computational cost with respect to atomistic simulations, the use of classical MD simulations with CG models preserving chemical specificity, such as the Martini force-field [57,58], has emerged as powerful strategy to tackle temporal evolution of biomolecular systems [59–61]. The use of a CG model reduces the number of particles in the simulated systems with a consequent decrease in the computational cost by 2–3 orders of magnitude compared to the atomistic models [62]. Moreover, the Martini force field has been already successfully used on CI [45,63,64]. The use of the P+ module for the accomplishment of the second aim of this study (see Introduction above) was justified by the observation that the mutations considered in our study affect different regions of the P module (two of them are close together and located in the ND6 and ND4L subunits, while the third mutation is located in the ND5 subunit, Fig. 1). In addition, we retained all the P+ module accessory subunits encoded by nDNA, as their removal would have exposed the NDx subunits to the membrane or the solvent in a non-physiological environment. Moreover, removing any of the NDx subunits could have caused instabilities within the P+ module itself. Finally, in addition to having a smaller number of atoms with respect to the complete CI structure, the P+ module has fewer technical difficulties because it does not bind the cofactors, that are in the N and Q modules.

The simulated systems were labeled with the letter "O" for ovine and "H" for human structures. The endings "op" and "cl" identified the open and closed conformation, respectively. The simulations consisted of: *i*) three 8 μs-long benchmark simulations on both the open and closed ovine P+ module structures (wtO^{op} and wtO^{cl} hereafter, respectively); *ii*) three 16 μs-long simulations performed on both the open and closed model structures of the *wild type* human P+ module (wtH^{op} and wtH^{cl}); and *iii*) three 16 μs-long simulations performed on the single p.M64V/ND6 mutant (m1) and on the triple p.M64V/ND6 - p.A71T/ND4L - p.T536A/ND5 mutant (m3). Even in the case of the mutated systems, the simulations were conducted on the model structures of both the open and closed human P+ module (namely: $m1H^{op}$, $m1H^{cl}$, $m3H^{op}$, and $m3H^{cl}$). The use of three replicas for each system is motivated by the observation that several simulations are more efficient for conformational space sampling than a single long trajectory [65]. A total of 336 μs of plain CG MD simulations were carried out.

2.2. The P+ module is stable in the microsecond time scale

Visual inspection of the trajectories revealed that there were no global unfolding processes throughout the simulation time. To analyze the overall behavior, the root mean square deviation (RMSD) of the

backbone beads (BB) was calculated for each subunit in the P+ module and plotted against simulation time (Figs. S2-S9). After the first four microseconds of MD simulation, all the RMSDs settle around a specific value in all systems (see Table S5). Consequently, all the following analysis were conducted by discarding the first 4 μs of simulation time. The ovine and the human replicas display a similar behavior throughout the simulation time, but the overall RMSD values are slightly higher in the second ones, reasonably because the human models have been derived from the ovine structures. The NDx subunits have generally the lowest average RMSD values and, consequently, are suitable for deeper analysis in terms of root mean square fluctuations (RMSF) and radius of gyration. As expected, loops, N- and C-terminals have higher RMSF values than the regions involved in secondary structure elements (Figs. S10-S17). The average RMSF were also calculated for each subunit of all systems (Table S8). Again, the NDx subunits have the lowest average RMSF values. As in the case of the deviations from the starting structures, the ovine replicas show slightly lower average RMSF values than the human replicas. These analyses show that the P+ module and

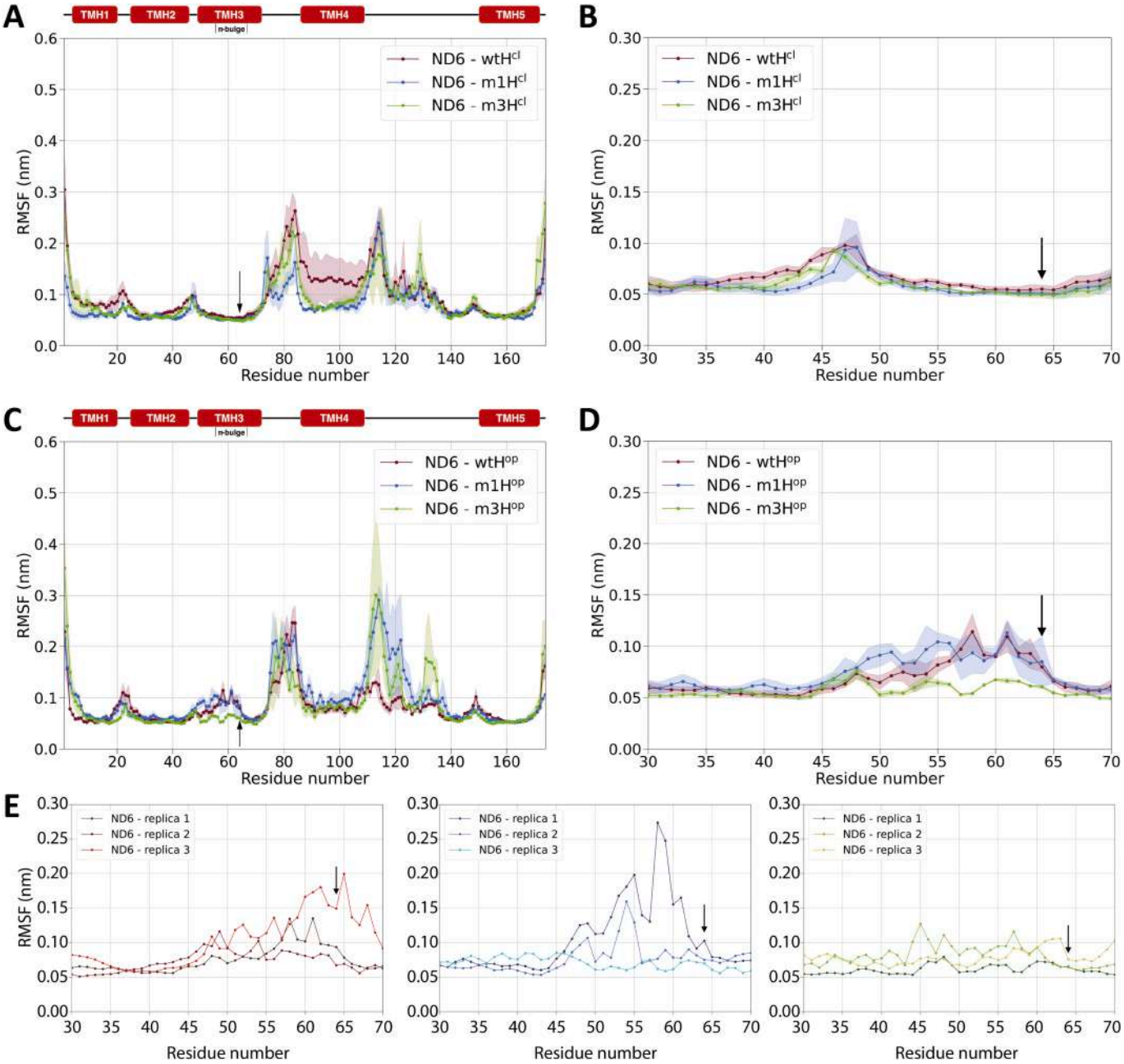

Fig. 2. RMSF of the human ND6 subunit in the open and closed conformation. (**A** and **C**) Average root mean square fluctuations (RMSF) values as a function of the residue number for ND6 in the human closed and open conformation, respectively. The *wild type* ND6 is shown in red, while the single and the triple mutants are shown in blue and green, respectively. The width of the shading indicates the standard deviation calculated on the three replicas of each simulation. The position of TMHs is indicated above the plots as is the position of the π-bulge in ND6 TMH3. (**B** and **D**) Details of the average RMSF in the p.M64V/ND6 region, which includes the C-terminal part of TMH2, TMH3 and the loop between them, for the human closed and open systems, respectively. (**E**) Detail of RMSF as a function of the residue number for each replica in the wild type (left panel), single mutant (middle panel) and triple mutant (right panel) in the same ND6 region shown in panels **B** and **D**. The wild type RMSF values are in different shades of red, while the single and triple mutants are in different shades of blue and green, respectively. In all panels, the position of the mutation is indicated by a black arrow. (For interpretation of the references to colour in this figure legend, the reader is referred to the web version of this article.)

its subunits are stable on the simulation time scale and that mutations do not produce easily detectable macroscopic effects on the protein complex. Furthermore, the modelled human structures show similar behavior to the experimental ovine structures, supporting the reliability of the computational setup. The radius of gyration remains constant for all NDx subunits throughout the simulation time (Figs. S18-S25), demonstrating that they remain compact on the time scale studied.

2.3. LHON-associated mutations do not affect the P+ module interactions with the membrane

Recent MD simulations [63,66] and high-resolution cryo-EM structures from different organisms [21,23,48,66–68] suggest that CI interacts with different lipids of the inner mitochondrial membrane. Among these, cardiolipin (CDL) seems to be involved in the activity and stabilization of CI [21,26,68,69]. Hence, an analysis of the distribution of the lipids around the protein has been performed and a density map of each lipid was calculated for all the simulated systems (Figs. S26-S33). This analysis confirmed that CDL mostly interacts at the interface between ND2-ND4 and ND4-ND5 and with the ND1 subunit [21,26,63,66]. Moreover, the maps show a higher density around the distal end of CI, suggesting that CDL may also bind ND5 subunit. Regarding the other lipids used to mimic the inner mitochondrial membrane, both palmitoyl-oleoyl-phosphatidylcholine (POPC) and palmitoyl-oleoyl-phosphatidylethanolamine (POPE) do not interact specifically with the P+ module, as no high-density regions were observed for these lipids. Conversely, palmitoyl-oleoyl-phosphatidylinositol (POPI) appears to settle around the P+ module with a density higher with respect to the bulk of the membrane. However, considering that POPI is interacting with all subunits, the latter interaction appears to be unspecific. Moreover, the lipid distributions are identical in the *wild type* and in the mutated systems. Consequently, the mutations studied do not cause changes in the interaction between the P+ module and the membrane.

2.4. The p.T536A/ND5 mutation does not affect the P+ module dynamics

A detailed analysis of the RMSF per residue calculated on the BB beads was performed on all NDx subunits, including a close-up of the regions around each of the three mutations (Fig. 2 and Figs. S34-S40). Specifically, the average RMSF values and the standard deviation were calculated on the three replicas of each system. Considering the spatial distance between the p.T536A/ND5 mutation and the others, this variant was firstly analyzed. The ND5 RMSF behavior of the human open and closed conformations is similar in the wild type and mutated systems (Fig. S37) and the comparison between the ovine ND5 fluctuations and those observed in the human models are superimposable (Fig. S40). Visual inspection and a contact analysis of all the residues found within a cut-off of 0.6 nm from each mutated residue show that the interaction network of p.T536A/ND5 with other residues in the ND5 subunit does not change significantly in both *wild type* and triple mutant systems. Indeed, p.T536A/ND5 interacts with residues that are not known to be involved in the function (Fig. S41). Consequently, we concluded that the p.T536A/ND5 mutation does not affect the P+ module dynamics and was excluded from further analysis.

2.5. P+ module fluctuations are affected by the p.M64V/ND6 mutation and worsened by the coexistence of the p.A71T/ND4L mutation

Considering the p.A71T/ND4L mutation, the RMSF analysis shows that the fluctuations of the region around this mutation in the *wild type* and the two mutated systems (single and triple) in both conformations are similar (Fig. S36). In the closed conformation, the RMSF of p.M64V/ND6 in the *wild type* and the two mutated systems does not show any effects either (Fig. 2A,B). However, in the open conformation, the *wild type* (wtH^{op}) and the single mutant ($m1H^{op}$) trajectories show a detectable increase to ca. 0.12 nm of the average fluctuations in the region between residues 45–65 of the ND6 subunit. This behavior is present also if one compares the ovine and human *wild type* systems. On the contrary, $m3H^{op}$ behaves similarly to the human systems in the closed conformation (Fig. 2C,D). Indeed, the average RMSF of the $m3H^{op}$ system is between 0.05 and 0.07 nm with a small standard deviation. Even two replicas of the $m1H^{op}$ system show very small RMSF in the region around the p.M64V/ND6 variant, while the third replica shows significantly larger values (Fig. 2E). In contrast, the RMSF values of the wtH^{op} system range between 0.08 and 0.20 nm for all three replicas. Consequently, it seems that the p.M64V/ND6 mutation alone affects the fluctuations of ND6 TMH3, while the presence of also the p.A71T/ND4L mutation in the triple mutant induces a more consistent change in the flexibility of the ND6 π-bulge (Fig. 2E).

Remarkably, visual inspection of the ND6 45–65 region and a cluster analysis conducted on the ND6 subunit (Figs. S42 and S43) revealed a striking different behavior between the simulations in open and closed conformation. In the latter, ND6 TMH3 is tightly folded and does not show significant conformational changes. On the other hand, in the open conformation, this region loses at least part of its secondary structure within the first 4 μs of simulation time in all replicas of each system. In the ND6 45–65 region, low RMSF values conceal two different behaviors: *i*) in the closed systems the RMSF trend is attributable to small fluctuations with respect to the starting structure; while *ii*) in the open conformation, two out of three replicas in $m1H^{op}$ and all the three $m3H^{op}$ replicas fluctuate less than all the wtH^{op} replicas. Interestingly, one of the $m1H^{op}$ replicas shows an RMSF behavior similar to the wtH^{op} replicas. A possible explanation of this behavior can be found in the way RMSF is calculated. Indeed, RMSF is a measure of the average displacement of each residue compared to the average structure calculated on the last 12 μs of each replica. This means that the replicas with lower RMSF values in the ND6 TMH3 region have smaller fluctuations compared to the average unfolded structure, which in turn is different from the folded starting structure. It could be thought that the π-bulge unfolding event is due to the CG representation adopted. However, another π-bulge located in ND1 TMH4 remains stable in all the replicas of every system. Moreover, other simulations have shown that CG π-helix fragments are stable in the time scale explored by our simulations [62]. For these reasons, the unfolding event must be due to something other than the level of detail of the simulations. Additionally, an analysis of the water beads in the ND6 TMH3 region (see SI) showed that unfolding is not caused by water insertion between ND6 helices. Consequently, the observed conformational transition is not a direct consequence of solvent exposure of regions that would normally be buried. Finally, visual inspection of the trajectories shows that the unfolding event of the ND6 TMH3 always starts from the loop connecting ND6 TMH3 and TMH4, which is in direct contact with the ubiquinone cavity of CI [21] and, in turn, with the Q module in the complete protein. This could mean that the ND6 TMH3 unfolding/refolding event could be somehow related to ubiquinone reduction (see Discussion below).

2.6. Estimation of p.M64V/ND6 and p.A71T/ND4L mutations effect

In order to provide a quantitative description of the effect caused by the primary p.M64V/ND6 mutation alone or in combination with the rare p.A71T/ND4L mutation, the origin of the different pattern of fluctuations in the *wild type* protein and the two mutants (single and triple) was explored. In particular, we focused on the π-bulge region by performing a set of analyses including: *i*) the study of the distances between residue pairs considering; *ii*) the backbone dihedral angles in ND6 TMH3; and *iii*) the interaction network formed by each of the mutated residues. A principal component (PC) analysis on the whole P+ module was not considered to be useful in view of the aim of the present investigation. In fact, the size of the P+ module would conceal the collective motions related to the mutations examined among a myriad of

other collective motions occurring on (presumably) much longer time scales.

2.6.1. Study of the distances between residue pairs

The time-evolving matrix of the distances between residue pairs within 0.7 nm from the point mutations p.M64V/ND6 was calculated for *wild type*, the single and triple mutant systems (see SI). This set is composed of 41 amino acids ("BB set" hereafter, Fig. 3A). An essential dynamics analysis performed on the time-distance matrix (see SI) [70,71] showed that the projections on the first three PC suffice to describe the overall dynamics of the region of interest (Fig. S44). The *wild type* system explores a wider range of conformations, while the triple mutant appears to be more rigid in both conformations (Fig. S44). Although it is not possible to distinguish between different conformational states, the fluid dynamics by which each conformation evolves into others within a single macro-state can be analyzed. Specifically, the network elasticity as a function of the lag-time can be estimated from the variance (see SI), which is roughly inversely proportional to the elasticity of the network. Fig. 3B shows the effect of point mutations on the variance of the network calculated as a function of the lag-time (τ), for open and closed systems. In general, the closed conformations are stiffer than the open ones. In particular, the $m3H^{cl}$ BB set is stiffer by 11 % than wtH^{cl} and $m1H^{cl}$ in a time scale comprised between pico- and nanoseconds. Considering that this effect is observed in the triple mutant only, it can then be ascribed to the presence of the p.A71T/ND4L variant together with p.M64V/ND6. On the other hand, the wtH^{op} system is more flexible and explores more states than $m1H^{op}$ and $m3H^{op}$ in a time scale longer than 0.1 μs. Indeed, $m1H^{op}$ and $m3H^{op}$ BB are similar and both ca. 20 % stiffer than the *wild type* system.

Therefore, the effect observed on the flexibility of the open conformation is ascribed to the p.M64V/ND6 mutation with only a small additional effect of the p.A71T/ND4L mutation in the triple mutant. To validate the previous result, a similar analysis was conducted using a slightly different set of residues and including the effect of side chains. To do so, the centers of mass (CM) of all the residues within 0.6 nm from p.M64V/ND6 together with the CM of the amino acids likely involved in the proton transfer (namely: Y142/ND1, E192/ND1, D66/ND3, E34/ND4L, E70/ND4L and A71T/ND4L) [21,25] were used to create the "CM set". The variance calculated as a function of the lag-time of the CM set network (Fig. 3C) agrees with the previous results (Fig. 3B). In the closed conformation, $m3H^{cl}$ is 38 % stiffer than wtH^{cl}, while in the open conformation both $m1H^{op}$ and $m3H^{op}$ are stiffer than wtH^{op} (20 % and 38 % respectively). In the open conformation $m3H^{op}$ is more rigid than the $m1H^{op}$, which, in turn, is significantly more rigid than the other systems.

2.6.2. Analysis of backbone dihedral angles in ND6 TMH3

To understand whether the different elasticity behavior of the ND6 π-bulge region can be ascribed to intra-helical or inter-helical interactions; two further analyses were performed. First, the intra-helical contribution was investigated by calculating the distribution of the dihedral angles (φ) formed by the ND6 TMH3 BB beads (residues 56–66), which probably plays a key role in the proton transfer [21]. In the closed conformation, the φ angles show a sharp distribution centered around 60°, a typical value of α-helices in the CG representation (Fig. S45). Consequently, the presence of p.M64V/ND6 mutation in the single and triple mutant and p.A71T/ND4L in the triple mutant do not induce any evident intra-helical conformational change in the closed systems. On the other hand, the φ dihedral distributions of the open systems show several conformations that are different from the typical ones of both α- or π-helices (Fig. 4). This is clearly a consequence of the unfolding event observed by visual inspection of the trajectories. The PC analysis conducted on the dihedral angles values (dihedral PCA) [72] can provide a measure of the conformational space explored by the π-bulge region in all systems. The total variance of the protein backbone, which is inversely proportional to the stiffness of the system, is reported in Table 1. Since the analysis of the RMSF showed that the individual replicas of the three open systems behaved differently (Fig. 2E), the dihedral PCA was performed on each replica. Two wtH^{op} replicas (namely replicas 1 and 3) as well as one $m1H^{op}$ replica (replica 1) has a larger variance than the other systems. In agreement with the RMSF observations, replica 1 of $m1H^{op}$ is the most flexible. However, the remaining $m1H^{op}$ and $m3H^{op}$ replicas are stiffer than the others, again in agreement with the RMSF observations. Looking at the average values of the cumulative variance in the three systems, p.M64V/ND6 mutant induces a partial stiffening of the π-bulge region, which is amplified by the presence of the p.A71T/ND4L change. Considering that the total variance gives information on the ability of the whole π-bulge region to switch from one conformational state to another, it is possible to explain why the three replicas of the $m3H^{op}$ system show small fluctuations compared to an average conformation that remains roughly unchanged throughout the simulation time (Fig. 2E). To confirm the latter result with a different approach, the variance of each separate conformational state was estimated by fitting with an apt number of Gaussian functions each peak observed in the φ dihedral angle distributions (Figs. S46-S54). The mean variance has been measured by averaging the half-height widths [σ(φ); i.e., the standard deviation] of all the Gaussian functions used in the fitting of each replica (Table 1). The trend of the average σ(φ) agrees with the results of the dihedral PCA analysis. This correlation suggests that: *i*) all the systems can explore a limited number of specific states and *ii*) a low mean variance of the states is associated with a low total variance and indicates that these systems cannot easily switch from one state to another in the time scale explored.

2.6.3. Interactions formed by each of the mutated residues

The inter-helical interactions were studied by considering all the residues found within a cut-off of 0.6 nm from each of the mutated residues. Figs. 5 and 6 show the fraction of simulation time of each residue found within the cut-off distance from amino acids 64 of ND6 and 71 of ND4L subunit, respectively. In the open conformation, the number of residues within the cut-off distance from amino acid 64 of ND6 subunit is larger than in the closed one (Fig. 5). This can be caused by the unfolding of ND6 TMH3. In fact, in the open conformation p.M64V/ND6 moves away from its initial position and comes closer to residues that otherwise would be too far in the folded structure. Therefore, the smaller number of residues within the cut-off distance in the closed conformation is probably caused by the stability of the secondary structure of the ND6 TMH3. Interestingly, many of the residues with greater residence time in the open conformation (i.e., ca. >30 %, Fig. 5) are found in all three systems studied (wtH^{op}, $m1H^{op}$ and $m3H^{op}$). Conversely, the residues with lower residence time (i.e., ca. <30 %) are found in only one of the three systems. This means that some of the residues within the cut-off in the wtH^{op} system are not observed in the two mutated systems and some residues are only found for $m1H^{op}$ and $m3H^{op}$. Due to the larger apolar character of valine compared to the *wild type* methionine (see SI) [57,62], it appears that p.M64V/ND6 mutation is able to form unspecific interactions with other hydrophobic residues and to settle in meta-stable conformational states upon unfolding. The specific conformation and the contacts established by p.M64V/ND6 mutation in each meta-stable state are peculiar for each replica. The distance analysis on the residues close to amino acid 71 of ND4L subunit shows that the number of residues is roughly maintained in both conformations (Fig. 6), coherently with the conformational stability of ND4L TMH3. Furthermore, the residence times involving this mutated residue are longer in both the triple mutant systems. Indeed, the sum of the residence times in the $m3H^{op}$ and $m3H^{cl}$ systems is significantly higher than in both the *wild type* and single mutant systems. This result is reasonably expected because threonine has a larger steric hinderance than alanine. Moreover, threonine contains a polar group in the side chain, that increases the polar character (see SI) [57,62]. Therefore, the mutated residue can form a higher number of interactions with other residues than alanine and, again, this observation can explain the

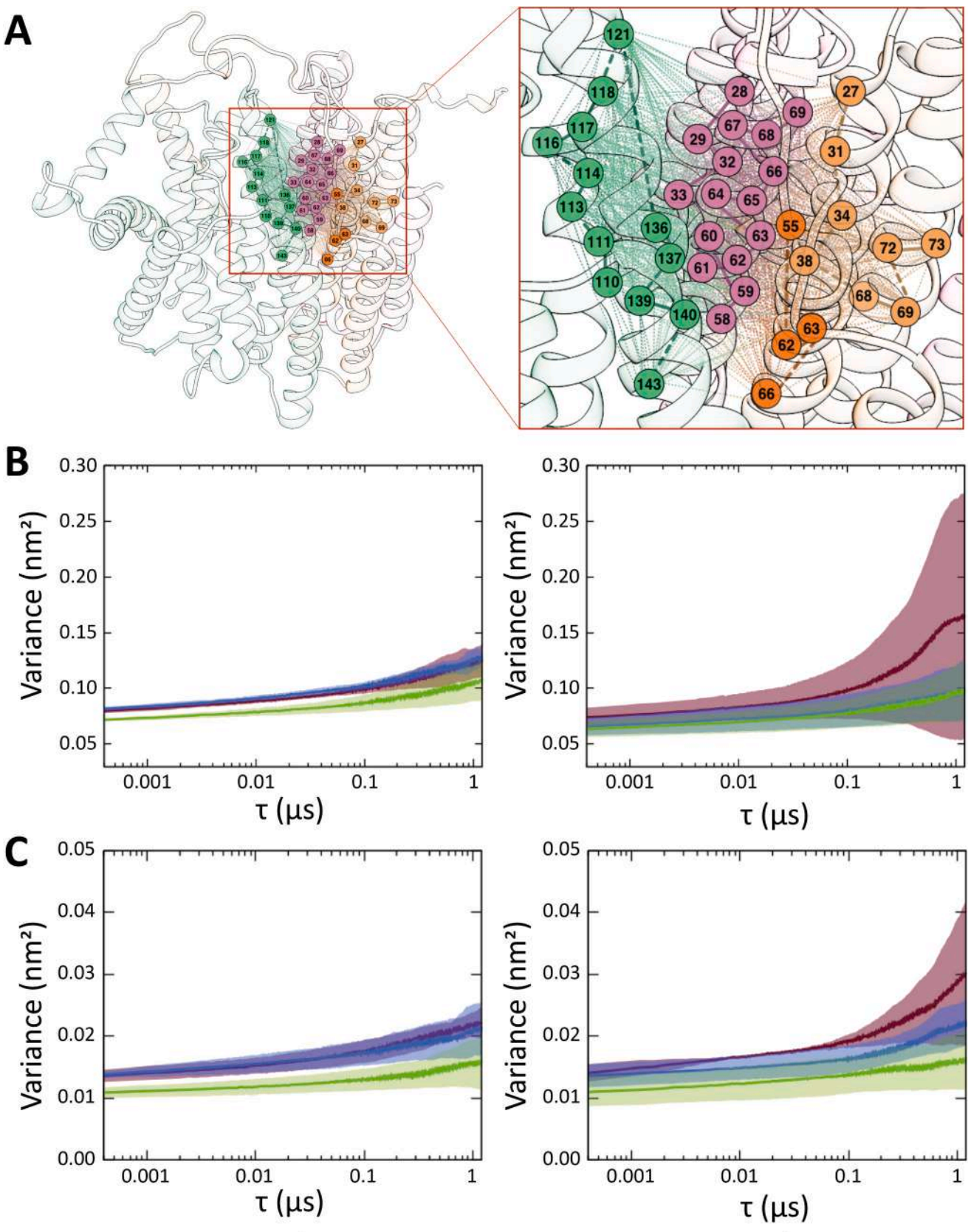

Fig. 3. Analysis of the time-evolving distance matrices in the p.M64V/ND6 region in the open and closed conformation. (**A**) P+ module region within 0.7 nm from p. M64V/ND6. The transparent ribbons of the ND1, ND3, ND4L and ND6 subunits are colored as in Fig. 1. (**B**, **C**) Variance of the network calculated as a function of the lag time (τ) in the closed (left panel) and open (right panel) systems, for the BB set (**B**) and for the CM set (**C**). In panels **B** and **C**, the *wild type* is shown in red, while the single and triple mutants are shown in blue and green, respectively. The standard deviation of the variance obtained by averaging over the three replica is shown as a shaded area. (For interpretation of the references to colour in this figure legend, the reader is referred to the web version of this article.)

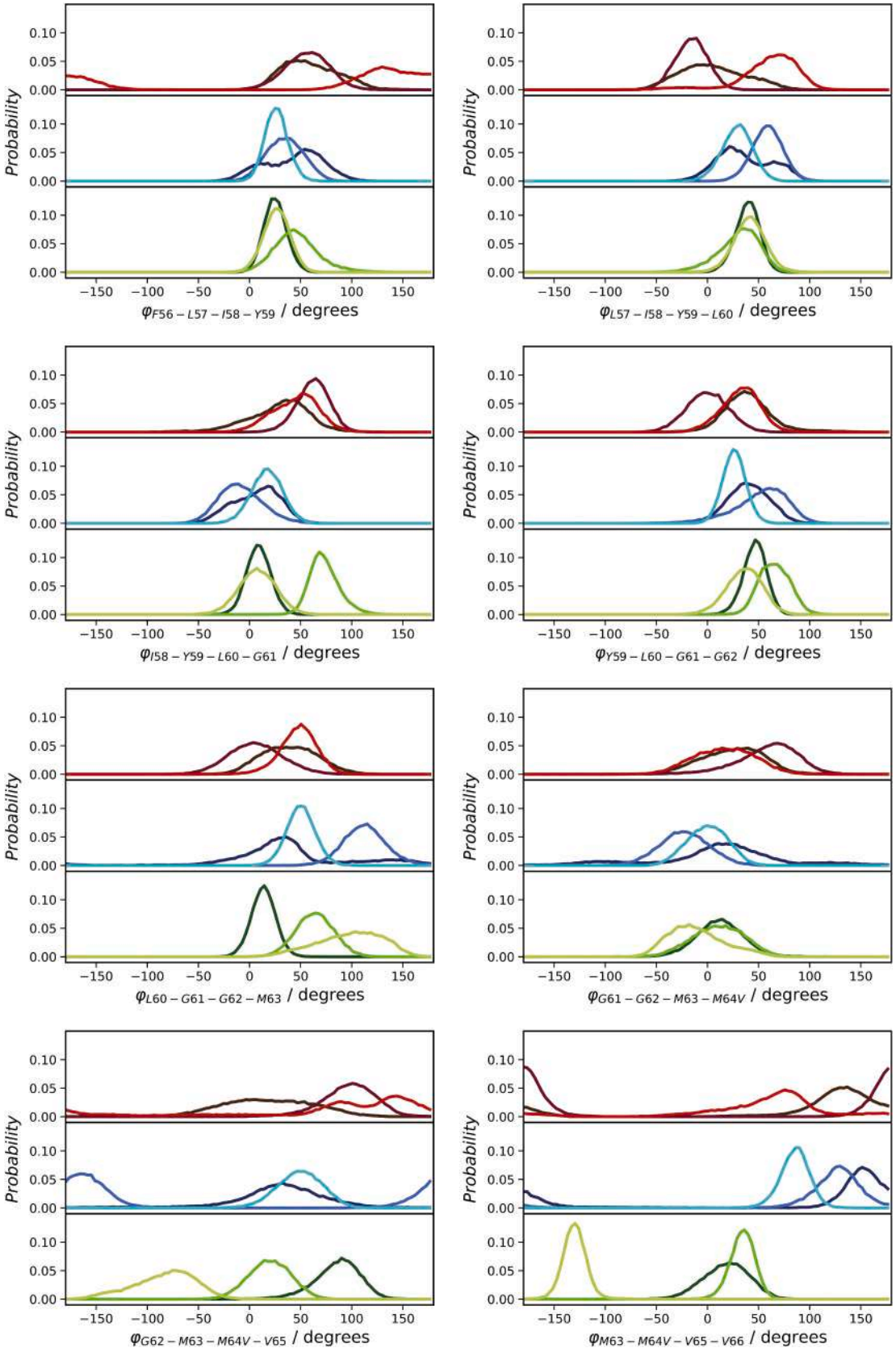

Fig. 4. Analysis of the BB dihedrals in the ND6 TMH3 π-bulge region in the open systems. Distribution of the backbone dihedral angles observed throughout the simulations in the open systems. The *wild type* dihedrals are in different shades of red, while the single and triple mutants are in different shades of blue and green, respectively. (For interpretation of the references to colour in this figure legend, the reader is referred to the web version of this article.)

Table 1
Total variance and average amplitude of the ND6 TMH3 BB dihedral angle distribution in the open systems. Total variance is calculated as the sum of the eigenvalues derived from the dihedral PCA analysis [72] and the average half-height widths [σ(φ), degrees] of the Gaussian curves used to fit the dihedral angle distributions in Figs. S28-S36). The last column shows the average values over the three replicas for each system.

System	Replica 1		Replica 2		Replica 3		Average	
	Total variance	Avg. σ(φ) (degrees)	Total variance	Avg. σ(φ) (degrees)	Total variance	Avg. σ(φ) (degrees)	Total variance	Avg. σ(φ) (degrees)
wtH^{op}	2.06	49	1.16	44	2.36	48	1.8 ± 0.6	47 ± 3
$m1H^{op}$	2.59	46	1.10	39	0.58	31	1.4 ± 1.0	40 ± 8
$m3H^{op}$	0.64	31	0.83	34	1.07	40	0.9 ± 0.2	35 ± 5

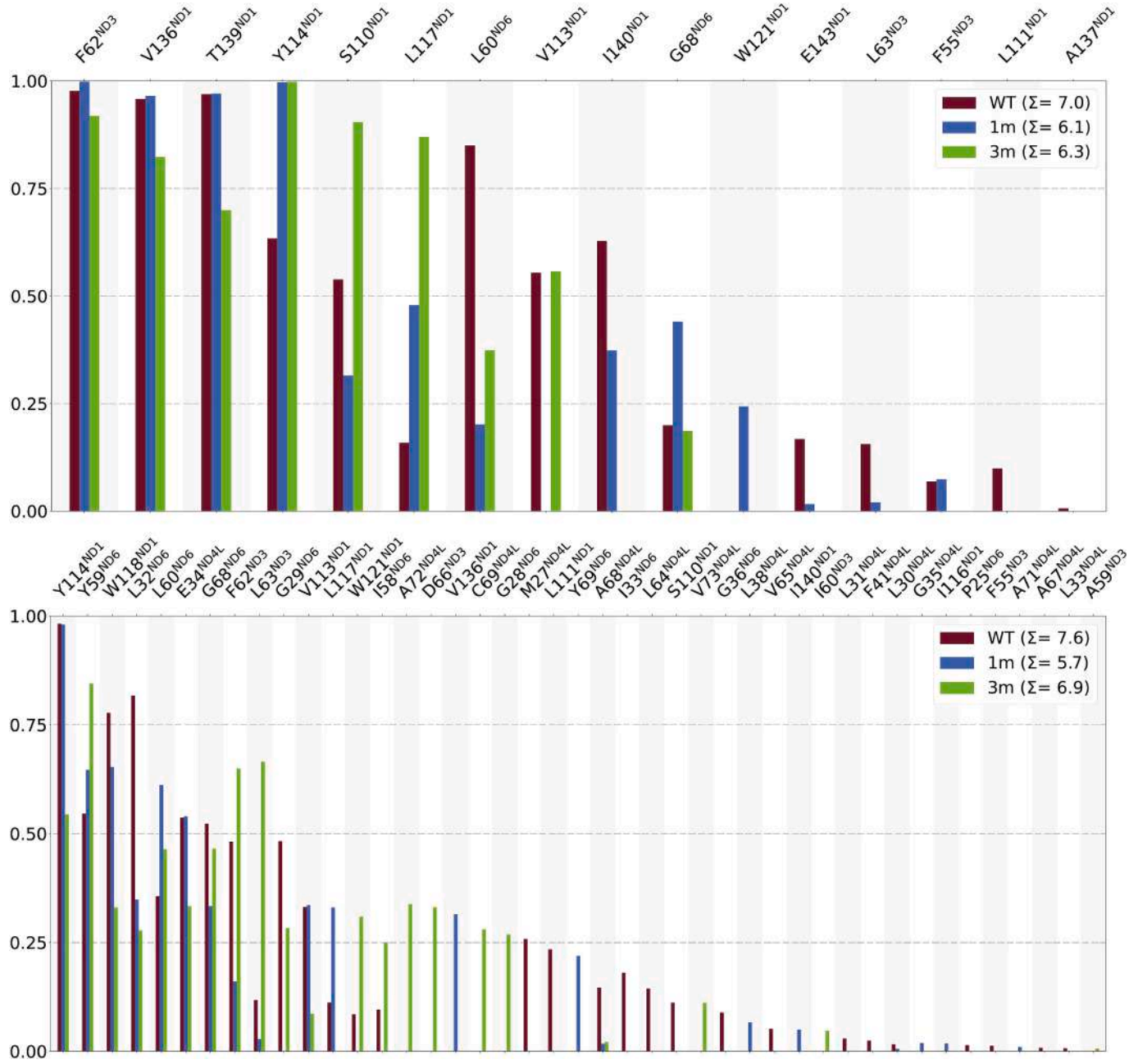

Fig. 5. Residues within 0.6 nm of p.M64V/ND6 and residence time within cut-off. Bars are colored in red, blue, and green for the *wild type*, single mutant, and triple mutant simulations, respectively. The height of the bars is proportional to the fraction of simulation time. The top and bottom panels refer to the simulations performed starting from the closed and the open conformation, respectively. The three residues on either side of p.M64V/ND6 in the ND6 sequence were excluded from the analysis. (For interpretation of the references to colour in this figure legend, the reader is referred to the web version of this article.)

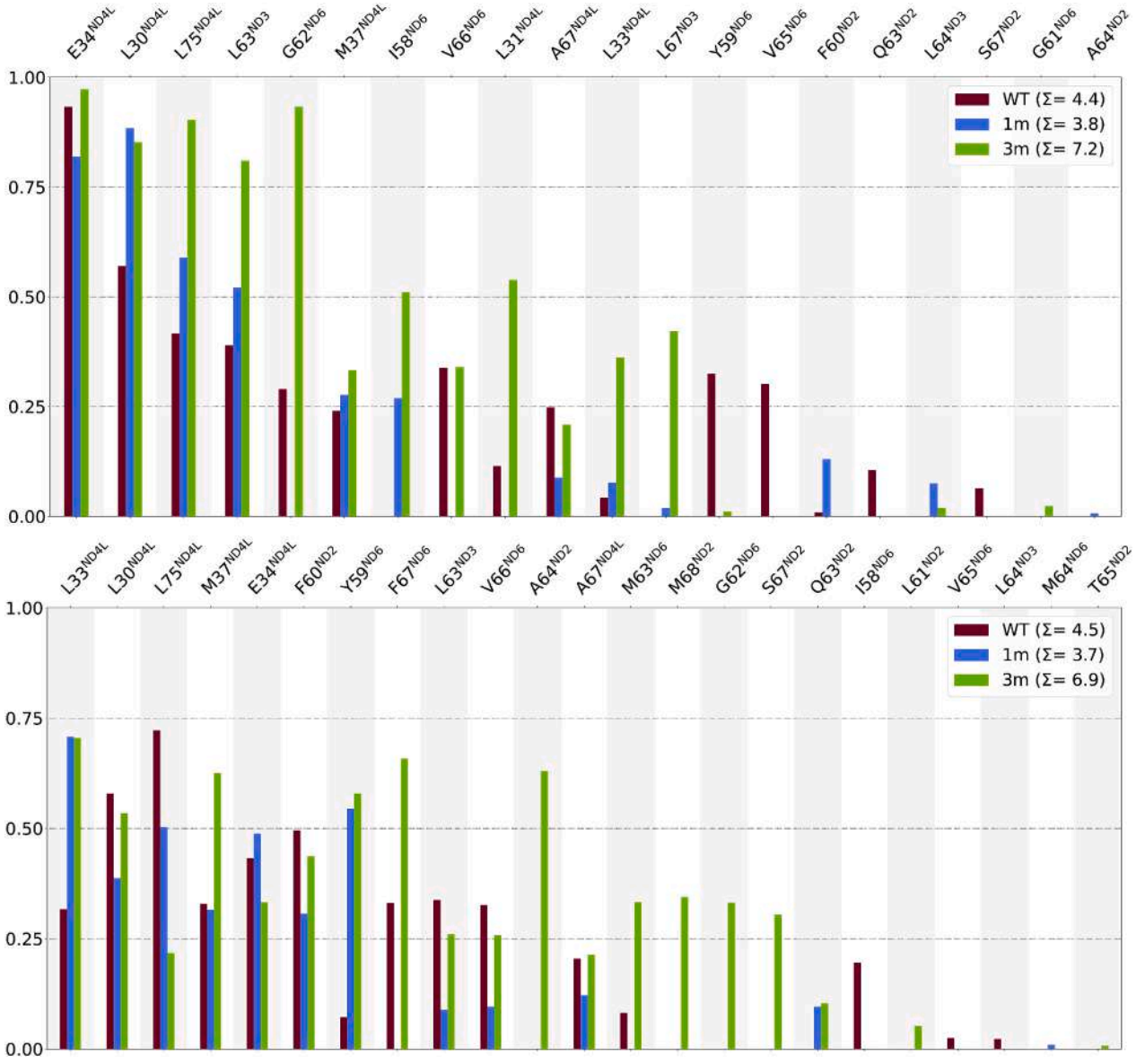

Fig. 6. Residues within 0.6 nm of p.A71T/ND4L and residence time within cut-off. Bars are colored in red, blue, and green for the *wild type*, single mutant, and triple mutant simulations, respectively. The height of the bars is proportional to the fraction of simulation time. The top and bottom panels refer to the simulations performed starting from the closed and the open conformation, respectively. The three residues on either side of p.A71T/ND4L in the ND4L sequence were excluded from the analysis. (For interpretation of the references to colour in this figure legend, the reader is referred to the web version of this article.)

stiffening in the distance network of both BB and CM sets in the triple mutant.

3. Discussion

This computational study investigated the structural and the dynamical effects of a primary CI pathogenic variant associated with LHON, namely m.14484T>C/*MT-ND6* (p.M64V/ND6), alone or in the concomitant presence of two additional rare variants: m.10680G>A/*MT-ND4L* (p.A71T/ND4L) and 13942A>G/*MT-ND5* (p.T536A/ND5). The aim of our study was to provide the proof of concept that a CG MD approach can be exploited to predict the impact of putatively pathogenic mtDNA variants, found alone or in combinations. For this purpose, the human P+ module was simulated in its *wild-type* form, with the inclusion of the primary variant (single mutant), and with a third system where the primary variant has been modelled together with the two rare variants (triple mutant). We here show that the presence of the p.M64V/ND6 mutation stiffens the dynamics of the P+ module in the putative E-channel (see below), while the p.A71T/ND4L mutation cooperates with the p.M64V/ND6 mutation, altering the conformational changes characterizing the open/closed states of CI. This phenomenon can affect CI efficiency in energy conservation by slowing down proton transport, that is compatible with the currently available biochemical investigations [10,11,73].

There are several rare CI variants that are confirmed as “primary” LHON pathogenic variants and peculiar combinations of individually non-pathogenic missense mtDNA variants in NDx genes for which the pathogenic potential role is supported by multiple evidence [12,74]. Among the three primary LHON variants, we selected the m.14484T>C/*MT-ND6* because it is a good example of a puzzling pathogenic variant that is present both in LHON and healthy population [15,16]. Indeed, when this variant is found in specific haplogroups and/or in combination with other rare variants, it causes LHON yet with varying degrees of penetrance [14,17] as opposed to a frequency of 1 in about 800–1000 individuals in the general population [16]. Then, we selected a peculiar pair of rare variants (m.10680G>A/*MT-ND4L* and m.13942A>G/*MT-*

ND5) which were reported in concomitance with the m.14484T>C/*MT-ND6* in a single Chinese family characterized by complete LHON penetrance, strongly suggesting their possible synergic effect in triggering the disease [17]. We thought this was the perfect example to exercise our approach in providing a "proof of principle". More specifically, the combination of variants considered in the present investigation is of interest because, in the protein, two of these three mutations are in the same CI region (the E-channel), while the third is in a completely different region.

In this work, tens of microsecond-long CG molecular dynamics simulations were carried out starting from the experimental ovine cryo-EM structure as well as on the human models of the CI P module with the addition of the NDUFS2/49 kDa (human/ovine subunits nomenclature). For all the systems, open and closed conformations, which correspond to two different stages of the proposed CI catalytic cycle, were considered. The human *wild type* models behave like the experimentally obtained ovine structures, confirming the reliability of the modelling procedure. The analysis of the simulations on the triple mutant suggested that the p.T536A/ND5 mutation does not affect the proton transfer and the protein function. This variant was never observed in LHON patients without the concomitant presence of other pathogenic variants. The p.T536A/ND5 mutation affects the ND5 subunit, while the latter is in contact with subunit ND4. Visual inspection of the trajectories and both the RMSD and RMSF analyses on the dynamics of these two subunits show that there are no significant changes in their secondary structure between closed and open system, as observed in previous experimental studies [21,24,28]. Then, the focus was placed on the remaining two mutations, p.M64V/ND6 and p.A71T/ND4L, the first present in both the single and triple mutant systems while the second has been included only in the triple mutant system. The p.M64V/ND6 and p.A71T/ND4L mutations are close to each other in the putative *E*-channel, a proton channel mainly constituted by glutamate residues (Fig. 1) composed of ND1, ND3, ND6 and ND4L subunits. The E-channel proposed function is to connect the ubiquinone site to the three antiporter-like subunits [21,25]. According to one of the CI catalytic cycle current hypotheses [21,25], the conformational transitions occurring in the E-channel region are crucial for CI function. The activity of the enzyme is probably associated also with a large conformational transition involving the Q and N modules together with other movements inside the P module. Specifically, the open-to-closed conformational transition involves, among other movements, the rearrangement of the ND6 TMH3 which takes shape through a conversion of a π-bulge fragment into an α-helix and ends up in a ND6 TMH3 rotation. Notably, the p.M64V/ND6 and p.A71T/ND4L mutations are located at the hinge between the P module and the remaining CI modules, specifically the former on ND6 TMH3 and the latter on ND4L TMH3. Indeed, the P module is proposed to be formed by four proton pumps connected by a nearly linear arrangement of conserved charged residues, called the hydrophilic axis. The E-channel is the initial part of the hydrophilic axis, with one side close to the Q-site and the other side proposed to be in the ND4L subunit. In the open conformation, the position of ND6 TMH3 closes the E-channel by placing M64/ND6 and F68/ND6 residues between two distinct clusters of water molecules. The conformational rearrangements leading to the closed conformation cause the rotation of ND6 TMH3, which in turn moves apart M64/ND6 and F68/ND6. This movement creates a continuous water wire buried inside the P module, connecting the Q-site to two ND4L conserved glutamate residues (E34 and E70) and generating a chain of events that ultimately lead to proton pumping.

To understand the possible cooperative effect of the p.A71T/ND4L mutation on the puzzling pathogenic p.M64V/ND6 mutation, the simulations conducted on the human *wild type* P+ module were compared with the simulations on the single mutant comprising only the p.M64V/ND6 mutation and the triple mutant system including all the mutations investigated here. The structural and multivariate analyses carried out on such simulations suggested that:

i) the p.M64V/ND6 and p.A71T/ND4L mutations induce a stiffening of the ND6 TMH3 π-bulge region with different effects on the open and closed conformations. In particular, the p.M64V/ND6 mutation affects the open conformation, while the additional presence of p.A71T/ND4L mutation has a detectable effect on both conformations.
ii) in the open conformation, the ND6 TMH3 unfolds in all the simulated systems, but the presence of one or both changes causes the persistence of specific meta-stable conformational states that are not present, on average, in the *wild type* system. Consequently, our simulations suggests that the π-to α-helix (and *vice versa*) conformational transitions occurs through a partial ND6 TMH3 unfolding and refolding process. This unfolding phenomenon has never been reported before for CI, but is not completely unexpected [75]. According to the catalytic mechanism proposed by Sazanov and coworkers [21], CI must undergo a conformational transition from open to closed conformations and *vice versa*. This involves a rearrangement of hydrogen bonds that stabilize the secondary structure of the protein in several regions, including also ND6 TMH3. Specifically, it seems that in the open to closed transition half of ND6 TMH3 rotates by about 180°. During such a conformational change, several hydrogen bonds are simultaneously broken, while the hydrogen bonds are broken one by one in the unfolding event of a helix. Consequently, the unfolding of ND6 TMH3 is more energetically favored than the ND6 TMH3 twisting. In other words, the present simulations indicate that the π-bulge can convert into an α-helix, and *vice versa*, through an unfolding/refolding event [75]. The presence of the mutations can slow down the ND6 TMH3 conformational rearrangement.

Hence, we conclude that these two phenomena may slow down and/or partially prevent the conformational transition from open to closed and *vice versa*, affecting the coupling between ubiquinone reduction and proton pumping in CI. In fact, even a slowing of the rotation of ND6 TM3 during the transition from open to closed can affect the formation of the water wire in the E-channel and, consequently, the sequence of events required for proton pumping. These results may explain the puzzling pathogenic or non-pathogenic effect of m.14484T>C/*MT-ND6* (p.M64V/ND6) variant in different mtDNA backgrounds, giving some clues about the role of rare variants in mitochondrially encoded subunits of CI. The combination of these rare aminoacidic changes may have and additive effect on the slight defect induced by m.14484T>C/*MT-ND6* (p.M64V/ND6), significantly decreasing oxidative phosphorylation efficiency with the consequent overall bioenergetic defect behind the disease.

The computational setup used here can be used for the systematic characterization and classification of CI mutations and population-specific non-synonymous variants, alone or in combinations, at a limited computational cost. While the functional effects of single variants can be relatively easily evaluated through biochemical investigations in cell models such as fibroblasts and cybrids, the outcomes of combinations of putatively pathogenic variants are more difficult to define, due to the lack of proper models. In this frame, this computational approach may overcome such experimental limitations, permitting an evaluation of all the possible combinations of mtDNA missense variants in CI genes. Moreover, these findings could be supported by the release of the high-resolution experimental structures of both *wild type* and mutated human CI. This would allow experimental validation of the observed changes in the network of interactions involving the ND6 TMH3 region. It would certainly be interesting to test our method on other rare variants, and it is our intention to use this tool for future studies in which other variants, alone or in combination, will be considered systematically. We believe that this computational approach would be useful to predict pathogenic and neutral interactions among variants to understand their potential synergistic effects, although we cannot predict the real biochemical effect on CI activity. In addition, the distance network in the p.M64V/ND6 region can be used to derive

appropriate collective variables to use in enhanced sampling calculations and speed up the open-to-close transition time scale. Finally, further use of cybrid cells can be fundamental to study and functionally validate the effect of the mutations studied here as well as other and new mutations or population-specific non-synonymous variants.

4. Methods

4.1. Reconstruction of unsolved regions in ovine P+ module structures

The solved cryo-EM structures of the CI P+ module from *O. aries* in both open (PDB id 6ZKA) [21] and closed conformation (PDB id 6ZKB) [21] were utilized as main template for the wtO^{op} and wtO^{cl} systems, respectively. The unsolved regions in the selected structures were reconstructed by using Modeller 10.0 [76]. In particular, the NDUFS2/49 kDa subunit was modelled using as template the ovine structures obtained from the enzyme flash-frozen while actively catalyzing NADH: decyl-ubiquinone oxidoreduction in the open (PDB id 6ZKE) [21] and closed conformation (PDB id 6ZKC) [21]. These structures were chosen for their higher resolution compared to the other ovine structures. See SI for additional details.

4.2. Homology modelling of human P+ module structures.

The *wild type* human structural models in both open and closed conformation were generated by using the optimized ovine structures as template and by using Modeller 10.0. The selected variants (p.M64V/ND6, p.A71T/ND4L and p.T536A/ND5) were created by using the *swapaa* tool included in UCSF Chimera 1.16 [77].

4.3. Phosphopantetheine CG mapping and parametrization

The acyl-carrier supernumerary subunits located in the Q and P modules covalently bind a molecule of phosphopantetheine (ZMP) each, which in turn stabilizes through its acyl chains the two supernumerary subunits NDUFAB1. ZMP prosthetic moiety is covalently linked via phosphodiester bond to Ser44 of the acyl carrier subunit. The ZMP molecule was parameterized according to Martini 2.2 procedure. See SI for further details.

4.4. Systems setup

The coarse-grained representation of the two ovine and the six P+ modules was built by using the *Martini Maker* tool [78,79] included in the CHARMM-GUI web server [80]. Each protein system was converted to the CG representation by using the Martini 2.2 force field [57,58] and then was embedded in a 300 × 300 Å bilayer membrane. The lipid composition was chosen to mimic the human inner mitochondrial membrane, with 40 % POPC, 30 % POPE, 16 % POPI and 14 % CDL [81]. The protein-membrane systems were, then, enclosed in a rectangular box with water and 0.15 M of Na^+ and Cl^- ions, plus counterions to ensure electroneutrality. The use of an elastic network (Elnedyn) was not implemented here to let the system evolve from the initial structure into different states. The obtained CG systems have approximately 144,000 beads each. A ZMP and an AMP molecule [82] were added *a posteriori* to each system removing overlapping solvent beads.

4.5. Systems minimization, equilibration, and production runs

Each system underwent two energy minimization and five restrained equilibration stages using GROMACS 2020.1 [83–85]. See SI for further details on minimization and equilibration. Production runs were performed by using the leap-frog algorithm with a time step of 20 fs and a temperature of 303.15 K. The temperature and the pressure of the systems were set by the velocity-rescale thermostat and the Parrinello-Rahman barostat [86]. Periodic boundaries were applied to the systems and the electrostatic interactions were calculated through the Particles Mesh Ewald method [87]. The cut-off values for the real part of the electrostatic interactions and for the van der Waals interactions were set to 1.1 nm.

4.6. Trajectory analysis

The simulated trajectories were analyzed with GROMACS tools and the Python packages MDAnalysis [88], MDTraj 1.9.8 [89], and mdciao 0.0.5 [90], using in-house Jupyter notebooks [91]. The analyses were performed at the CG level, considering the approximations introduced by such a representation. However, back-mapping to the all-atom level is also an approximation, since after positioning the back-mapped atoms, a minimization and equilibration procedure is still required to obtain a reasonable all-atom structure. In addition, the size of the system under study makes the back-mapping procedure more error-prone. In the RMSD analyses, the CG representation obtained from the initial cryo-EM structures in were considered as reference. Lipids density maps (see Figs. S26-S33) were carried out using the GROMACS *densmap* tool, and the plots were generated using *Gnuplot* (http://www.gnuplot.info). The upper and lower membrane leaflets, named Matrix and IMS, respectively, were defined as the volume slices (along the axis perpendicular to the membrane) between the center of mass of the membrane and the POPC, CDL2, POPI and POPE heads. Other plots were generated with matplotlib library [92]. UCSF Chimera 1.16 [77] and UCSF ChimeraX 1.5 [93] were used for the molecular figures. The dihedral angles distributions were analyzed by using the dihedral PCA procedure [72]. The cluster analysis on the ND6 subunit was performed in accordance with the gromos algorithm [94] summing the replicas of each system to increase conformational space sampling and using a cut-off of 0.15 nm.

4.7. Data availability

The trajectories are available to any researcher for purposes of reproducing or extending the analysis and are deposited in Zenodo [95].

4.8. Limitations

By grouping atoms together, a CG model reduces the degrees of freedom and, consequently, the computational cost of the simulations and their analysis [96]. Moreover, the dynamics of a CG system are enhanced through the elimination of additional friction and noise that are present in an atomistic representation. These features make CG representation ideal for dealing with a protein complex of the size of the CI or even just its P+ module. The reduction in the number of degrees of freedom causes a change in the inter-residue interaction scheme as this occurs between beads and no longer between atomistic functional groups.

The absence of the N and Q modules might introduce some artifacts and structural reorganization or accelerate/make impossible certain events that take place during the catalytic cycle. For example, the use of only the P+ module has probably made faster the unfolding of the ND6 TMH3 π-bulge in the open conformation and may have prevented its refolding. On the other hand, the time scale of the open/closed transition – and *vice versa* – is likely to be greater than the one considered in the simulations reported here. However, the aim of the present investigation was to study the overall structural and dynamical effects of three specific mutations and not to draw conclusions on mechanistic aspects, for which much longer time scales and atomistic details are required.

Finally, when the simulations reported here were already in progress, a new version of Martini force field (Martini 3) [97] was released. The new force field includes improved interaction parameters, additional bead types and the inclusion of additional interactions such as hydrogen bonds and electronic polarizability. It would possibly be interesting to repeat the simulations reported here using Martini 3.

Declaration of competing interest

None.

Data availability

The trajectories are available to any researcher for purposes of reproducing or extending the analysis and are deposited in Zenodo (https://doi.org/10.5281/zenodo.10355270)

Acknowledgments

The authors thank Giorgio Turtù for technical help and insightful discussions.

Funding sources

This investigation was supported by #NEXTGENERATIONEU (NGEU) and funded by the Ministry of University and Research (MUR), through the RFO grant 2020 and the National Recovery and Resilience Plan (NRRP), project MNESYS (PE0000006) – A Multiscale integrated approach to the study of the nervous system in health and disease (DN. 1553 11.10.2022). FM was supported also by Consorzio Interuniversitario Risonanze Magnetiche di Metallo Proteine (CIRMMP). We acknowledge the CINECA award under the ISCRA initiative, for the availability of high-performance computing resources and support.

CReDiT authorship contribution statement

The manuscript was written through contributions of all authors. All authors have given approval to the final version of the manuscript. Conceptualization: LR, FL, LC, LI, AMG, FM. Data curation: LR, FL, FM. Formal analysis: LR, FL, AB, JF, FM. Funding acquisition: FL, FZ, FM. Methodology: LR, FL, AB, JF, FM. Investigation: LR, FL, AB, JF, FM. Project administration: FL, LC, FZ, LI, VC, AMG, FM. Resources: FL, FM. Software: LR, FL, AB, JF, FM. Visualization: LR, FL, AB, JF, FM. Verification: FL, FM. Supervision: FL, FM. Writing—original draft: LR, FL, LC, AB, JF, FZ, LI, VC, AMG, FM. Writing—review & editing: LR, FL, LC, AB, JF, FZ, LI, VC, AMG, FM.

Appendix A. Supplementary data

Supplementary data to this article can be found online at https://doi.org/10.1016/j.ijbiomac.2024.133086.

References

[1] E. Galemou Yoga, H. Angerer, K. Parey, V. Zickermann, Respiratory complex I - mechanistic insights and advances in structure determination, Biochim Biophys Acta Bioenerg 1861 (3) (2020) 148153.
[2] K. Parey, C. Wirth, J. Vonck, V. Zickermann, Respiratory complex I - structure, mechanism and evolution, Curr. Opin. Struct. Biol. 63 (2020) 1–9.
[3] S. Guerrero-Castillo, F. Baertling, D. Kownatzki, H.J. Wessels, S. Arnold, U. Brandt, L. Nijtmans, The assembly pathway of mitochondrial respiratory chain complex I, Cell Metab. 25 (1) (2017) 128–139.
[4] L.E. Formosa, M.G. Dibley, D.A. Stroud, M.T. Ryan, Building a complex complex: assembly of mitochondrial respiratory chain complex I, Semin. Cell Dev. Biol. 76 (2018) 154–162.
[5] A. Padavannil, M.G. Ayala-Hernandez, E.A. Castellanos-Silva, J.A. Letts, The mysterious multitude: structural perspective on the accessory subunits of respiratory complex I, Front. Mol. Biosci. 8 (2021) 798353.
[6] C.R. Ferreira, S. Rahman, M. Keller, J. Zschocke, I.A. Group, An international classification of inherited metabolic disorders (ICIMD), J. Inherit. Metab. Dis. 44 (1) (2021) 164–177.
[7] D.C. Wallace, G. Singh, M.T. Lott, J.A. Hodge, T.G. Schurr, A.M. Lezza, L. J. Elsas 2nd, E.K. Nikoskelainen, Mitochondrial DNA mutation associated with Leber's hereditary optic neuropathy, Science 242 (4884) (1988) 1427–1430.
[8] N.J. Newman, P. Yu-Wai-Man, V. Biousse, V. Carelli, Understanding the molecular basis and pathogenesis of hereditary optic neuropathies: towards improved diagnosis and management, Lancet Neurol. 22 (2) (2023) 172–188.
[9] N. Jurkute, P. Yu-Wai-Man, Leber hereditary optic neuropathy: bridging the translational gap, Curr. Opin. Ophthalmol. 28 (5) (2017) 403–409.
[10] M.D. Brown, I.A. Trounce, A.S. Jun, J.C. Allen, D.C. Wallace, Functional analysis of lymphoblast and cybrid mitochondria containing the 3460, 11778, or 14484 Leber's hereditary optic neuropathy mitochondrial DNA mutation, J. Biol. Chem. 275 (51) (2000) 39831–39836.
[11] A. Achilli, L. Iommarini, A. Olivieri, M. Pala, B. Hooshiar Kashani, P. Reynier, C. La Morgia, M.L. Valentino, R. Liguori, F. Pizza, P. Barboni, F. Sadun, A.M. De Negri, M. Zeviani, H. Dollfus, A. Moulignier, G. Ducos, C. Orssaud, D. Bonneau, V. Procaccio, B. Leo-Kottler, S. Fauser, B. Wissinger, P. Amati-Bonneau, A. Torroni, V. Carelli, Rare primary mitochondrial DNA mutations and probable synergistic variants in Leber's hereditary optic neuropathy, PloS One 7 (8) (2012) e42242.
[12] L. Caporali, L. Iommarini, C. La Morgia, A. Olivieri, A. Achilli, A. Maresca, M. L. Valentino, M. Capristo, F. Tagliavini, V. Del Dotto, C. Zanna, R. Liguori, P. Barboni, M. Carbonelli, V. Cocetta, M. Montopoli, A. Martinuzzi, G. Cenacchi, G. De Michele, F. Testa, A. Nesti, F. Simonelli, A.M. Porcelli, A. Torroni, V. Carelli, Peculiar combinations of individually non-pathogenic missense mitochondrial DNA variants cause low penetrance Leber's hereditary optic neuropathy, PLoS Genet. 14 (2) (2018) e1007210.
[13] D.C. Wallace, Mitochondrial DNA variation in human radiation and disease, Cell 163 (1) (2015) 33–38.
[14] G. Hudson, V. Carelli, L. Spruijt, M. Gerards, C. Mowbray, A. Achilli, A. Pyle, J. Elson, N. Howell, C. La Morgia, M.L. Valentino, K. Huoponen, M.L. Savontaus, E. Nikoskelainen, A.A. Sadun, S.R. Salomao, R. Belfort Jr., P. Griffiths, P. Yu-Wai-Man, R.F. de Coo, R. Horvath, M. Zeviani, H.J. Smeets, A. Torroni, P.F. Chinnery, Clinical expression of Leber hereditary optic neuropathy is affected by the mitochondrial DNA-haplogroup background, Am. J. Hum. Genet. 81 (2) (2007) 228–233.
[15] E.C. Watson, R.L. Davis, S. Ravishankar, J. Copty, S. Kummerfeld, C.M. Sue, Low disease risk and penetrance in Leber hereditary optic neuropathy, Am. J. Hum. Genet. 110 (1) (2023) 166–169.
[16] D.A. Mackey, J.S. Ong, S. MacGregor, D.C. Whiteman, J.E. Craig, M.I.G. Lopez Sanchez, L.S. Kearns, S.E. Staffieri, L. Clarke, M.B. McGuinness, W. Meteoukki, S. Samuel, J.B. Ruddle, C. Chen, C.L. Fraser, J. Harrison, N. Howell, A.W. Hewitt, Is the disease risk and penetrance in Leber hereditary optic neuropathy actually low? Am. J. Hum. Genet. 110 (1) (2023) 170–176.
[17] J. Yang, Y. Zhu, Y. Tong, Z. Zhang, L. Chen, S. Chen, Z. Cao, C. Liu, J. Xu, X. Ma, The novel G10680A mutation is associated with complete penetrance of the LHON/T14484C family, Mitochondrion 9 (4) (2009) 273–278.
[18] N. Howell, I. Kubacka, M. Xu, D.A. McCullough, Leber hereditary optic neuropathy: involvement of the mitochondrial ND1 gene and evidence for an intragenic suppressor mutation, Am. J. Hum. Genet. 48 (5) (1991) 935–942.
[19] D. Mackey, N. Howell, A variant of Leber hereditary optic neuropathy characterized by recovery of vision and by an unusual mitochondrial genetic etiology, Am. J. Hum. Genet. 51 (6) (1992) 1218–1228.
[20] V. Carelli, F.N. Ross-Cisneros, A.A. Sadun, Mitochondrial dysfunction as a cause of optic neuropathies, Prog. Retin. Eye Res. 23 (1) (2004) 53–89.
[21] D. Kampjut, L.A. Sazanov, The coupling mechanism of mammalian respiratory complex I, Science 370 (6516) (2020).
[22] H.R. Bridges, J.N. Blaza, Z. Yin, I. Chung, M.N. Pollak, J. Hirst, Structural basis of mammalian respiratory complex I inhibition by medicinal biguanides, Science 379 (6630) (2023) 351–357.
[23] I. Chung, J.J. Wright, H.R. Bridges, B.S. Ivanov, O. Biner, C.S. Pereira, G. M. Arantes, J. Hirst, Cryo-EM structures define ubiquinone-10 binding to mitochondrial complex I and conformational transitions accompanying Q-site occupancy, Nat. Commun. 13 (1) (2022) 2758.
[24] V. Kravchuk, O. Petrova, D. Kampjut, A. Wojciechowska-Bason, Z. Breese, L. Sazanov, A universal coupling mechanism of respiratory complex I, Nature 609 (7928) (2022) 808–814.
[25] V. Kravchuk, L. Sazanov, Structural investigation of E. Coli complex I as a mechanistic model, Biochimica et Biophysica Acta (BBA) -, Bioenergetics 1863 (2022) 148658.
[26] K. Parey, J. Lasham, D.J. Mills, A. Djurabekova, O. Haapanen, E.G. Yoga, H. Xie, W. Kuhlbrandt, V. Sharma, J. Vonck, V. Zickermann, High-resolution structure and dynamics of mitochondrial complex I-insights into the proton pumping mechanism, Sci. Adv. 7 (46) (2021) eabj3221.
[27] C. Hunte, V. Zickermann, U. Brandt, Functional modules and structural basis of conformational coupling in mitochondrial complex I, Science 329 (5990) (2010) 448–451.
[28] L.A. Sazanov, From the 'black box' to 'domino effect' mechanism: what have we learned from the structures of respiratory complex I, Biochem. J. 480 (5) (2023) 319–333.
[29] R.G. Efremov, R. Baradaran, L.A. Sazanov, The architecture of respiratory complex I, Nature 465 (7297) (2010) 441–445.
[30] J. Gutierrez-Fernandez, K. Kaszuba, G.S. Minhas, R. Baradaran, M. Tambalo, D. T. Gallagher, L.A. Sazanov, Key role of quinone in the mechanism of respiratory complex I, Nat. Commun. 11 (1) (2020) 4135.
[31] I. Chung, D.N. Grba, J.J. Wright, J. Hirst, Making the leap from structure to mechanism: are the open states of mammalian complex I identified by cryoEM resting states or catalytic intermediates? Curr. Opin. Struct. Biol. 77 (2022) 102447.
[32] D.N. Grba, I. Chung, H.R. Bridges, A.A. Agip, J. Hirst, Investigation of hydrated channels and proton pathways in a high-resolution cryo-EM structure of mammalian complex I, Sci. Adv. 9 (31) (2023) eadi1359.
[33] H. Kim, P. Saura, M.C. Poverlein, A.P. Gamiz-Hernandez, V.R.I. Kaila, Quinone catalysis modulates proton transfer reactions in the membrane domain of respiratory complex I, J. Am. Chem. Soc. 145 (31) (2023) 17075–17086.

[34] V.R. Kaila, M. Wikstrom, G. Hummer, Electrostatics, hydration, and proton transfer dynamics in the membrane domain of respiratory complex I, Proc. Natl. Acad. Sci. U. S. A. 111 (19) (2014) 6988–6993.
[35] V. Sharma, G. Belevich, A.P. Gamiz-Hernandez, T. Rog, I. Vattulainen, M. L. Verkhovskaya, M. Wikstrom, G. Hummer, V.R. Kaila, Redox-induced activation of the proton pump in the respiratory complex I, Proc. Natl. Acad. Sci. U. S. A. 112 (37) (2015) 11571–11576.
[36] P. Tan, Z. Feng, L. Zhang, T. Hou, Y. Li, The mechanism of proton translocation in respiratory complex I from molecular dynamics, J. Recept. Signal Transduct. Res. 35 (2) (2015) 170–179.
[37] A. Di Luca, A.P. Gamiz-Hernandez, V.R.I. Kaila, Symmetry-related proton transfer pathways in respiratory complex I, Proc. Natl. Acad. Sci. U. S. A. 114 (31) (2017) E6314–E6321.
[38] O. Haapanen, V. Sharma, Role of water and protein dynamics in proton pumping by respiratory complex I, Sci. Rep. 7 (1) (2017) 7747.
[39] J. Warnau, V. Sharma, A.P. Gamiz-Hernandez, A. Di Luca, O. Haapanen, I. Vattulainen, M. Wikstrom, G. Hummer, V.R.I. Kaila, Redox-coupled quinone dynamics in the respiratory complex I, Proc. Natl. Acad. Sci. U. S. A. 115 (36) (2018) E8413–E8420.
[40] E. Galemou Yoga, O. Haapanen, I. Wittig, K. Siegmund, V. Sharma, V. Zickermann, Mutations in a conserved loop in the PSST subunit of respiratory complex I affect ubiquinone binding and dynamics, Biochim. Biophys. Acta Bioenerg. 1860 (7) (2019) 573–581.
[41] O. Haapanen, A. Djurabekova, V. Sharma, Role of second Quinone binding site in proton pumping by respiratory complex I, Front. Chem. 7 (2019) 221.
[42] M. Hoias Teixeira, G., Menegon Arantes, balanced internal hydration discriminates substrate binding to respiratory complex I, Biochim Biophys Acta Bioenerg 1860 (7) (2019) 541–548.
[43] P. Saura, V.R.I. Kaila, Molecular dynamics and structural models of the cyanobacterial NDH-1 complex, Biochim Biophys Acta Bioenerg 1860 (3) (2019) 201–208.
[44] P. Saura, V.R.I. Kaila, Energetics and dynamics of proton-coupled Electron transfer in the NADH/FMN site of respiratory complex I, J. Am. Chem. Soc. 141 (14) (2019) 5710–5719.
[45] H.R. Bridges, J.G. Fedor, J.N. Blaza, A. Di Luca, A. Jussupow, O.D. Jarman, J. J. Wright, A.A. Agip, A.P. Gamiz-Hernandez, M.M. Roessler, V.R.I. Kaila, J. Hirst, Structure of inhibitor-bound mammalian complex I, Nat. Commun. 11 (1) (2020) 5261.
[46] C. Gupta, U. Khaniya, C.K. Chan, F. Dehez, M. Shekhar, M.R. Gunner, L. Sazanov, C. Chipot, A. Singharoy, Charge transfer and chemo-mechanical coupling in respiratory complex I, J. Am. Chem. Soc. 142 (20) (2020) 9220–9230.
[47] M.E. Muhlbauer, P. Saura, F. Nuber, A. Di Luca, T. Friedrich, V.R.I. Kaila, Water-gated proton transfer dynamics in respiratory complex I, J. Am. Chem. Soc. 142 (32) (2020) 13718–13728.
[48] I. Chung, R. Serreli, J.B. Cross, M.E. Di Francesco, J.R. Marszalek, J. Hirst, Cork-in-bottle mechanism of inhibitor binding to mammalian complex I, Sci. Adv. 7 (20) (2021).
[49] V.R.I. Kaila, Resolving chemical dynamics in biological energy conversion: long-range proton-coupled Electron transfer in respiratory complex I, Acc. Chem. Res. 54 (24) (2021) 4462–4473.
[50] M. Ropke, D. Riepl, P. Saura, A. Di Luca, M.E. Muhlbauer, A. Jussupow, A. P. Gamiz-Hernandez, V.R.I. Kaila, Deactivation blocks proton pathways in the mitochondrial complex I, Proc. Natl. Acad. Sci. U. S. A. 118 (29) (2021).
[51] N. Dhananjayan, P. Wang, I. Leontyev, A.A. Stuchebrukhov, Quinone binding in respiratory complex I: going through the eye of a needle, The squeeze-in mechanism of passing the narrow entrance of the quinone site, Photochem Photobiol Sci 21 (1) (2022) 1–12.
[52] Y. Lee, O. Haapanen, A. Altmeyer, W. Kuhlbrandt, V. Sharma, V. Zickermann, Ion transfer mechanisms in Mrp-type antiporters from high resolution cryoEM and molecular dynamics simulations, Nat. Commun. 13 (1) (2022) 6091.
[53] J. Lasham, O. Haapanen, V. Zickermann, V. Sharma, Tunnel dynamics of quinone derivatives and its coupling to protein conformational rearrangements in respiratory complex I, Biochim Biophys Acta Bioenerg 1864 (2) (2023) 148951.
[54] C.S. Pereira, M.H. Teixeira, D.A. Russell, J. Hirst, G.M. Arantes, Mechanism of rotenone binding to respiratory complex I depends on ligand flexibility, Sci. Rep. 13 (1) (2023) 6738.
[55] F. Guo, H. Yang, S. Li, Y. Jiang, X. Bai, C. Hu, W. Li, W. Han, Using Gaussian accelerated molecular dynamics combined with Markov state models to explore the mechanism of action of new oral inhibitors on complex I, Comput. Biol. Med. 108598 (2024).
[56] J.T. Fuller 3rd, S. Barnes, L.A. Sadun, P. Ajmera, A.N. Alexandrova, A.A. Sadun, Coenzyme Q10 trapping in mitochondrial complex I underlies Leber's hereditary optic neuropathy, Proc. Natl. Acad. Sci. U. S. A. 120 (39) (2023) e2304884120.
[57] S.J. Marrink, H.J. Risselada, S. Yefimov, D.P. Tieleman, A.H. de Vries, The MARTINI force field: coarse grained model for biomolecular simulations, J. Phys. Chem. B 111 (27) (2007) 7812–7824.
[58] D.H. de Jong, G. Singh, W.F. Bennett, C. Arnarez, T.A. Wassenaar, L.V. Schafer, X. Periole, D.P. Tieleman, S.J. Marrink, Improved parameters for the Martini coarse-grained protein force field, J. Chem. Theory Comput. 9 (1) (2013) 687–697.
[59] R.A. Corey, W. Song, A.L. Duncan, T.B. Ansell, M.S.P. Sansom, P.J. Stansfeld, Identification and assessment of cardiolipin interactions with E. Coli inner membrane proteins, Sci. Adv. 7 (34) (2021).
[60] H.I. Ingolfsson, C.A. Lopez, J.J. Uusitalo, D.H. de Jong, S.M. Gopal, X. Periole, S. J. Marrink, The power of coarse graining in biomolecular simulations, Wiley Interdiscip Rev Comput Mol Sci 4 (3) (2014) 225–248.
[61] S. Salassi, F. Simonelli, A. Bartocci, G. Rossi, A Martini coarse-grained model of the calcein fluorescent dye, J. Phys. D Appl. Phys. 51 (38) (2018) 384002.
[62] L. Monticelli, S.K. Kandasamy, X. Periole, R.G. Larson, D.P. Tieleman, S.J. Marrink, The MARTINI coarse-grained force field: extension to proteins, J Chem Theory Comput 4 (5) (2008) 819–834.
[63] A. Jussupow, A. Di Luca, V.R.I. Kaila, How cardiolipin modulates the dynamics of respiratory complex I, Sci. Adv. 5 (3) (2019) eaav1850.
[64] P. Wang, I. Leontyev, A.A. Stuchebrukhov, Mechanical allosteric couplings of redox-induced conformational changes in respiratory complex I, J. Phys. Chem. B 126 (22) (2022) 4080–4088.
[65] B. Knapp, L. Ospina, C.M. Deane, Avoiding false positive conclusions in molecular simulation: the importance of replicas, J Chem Theory Comput 14 (12) (2018) 6127–6138.
[66] K. Parey, O. Haapanen, V. Sharma, H. Kofeler, T. Zullig, S. Prinz, K. Siegmund, I. Wittig, D.J. Mills, J. Vonck, W. Kuhlbrandt, V. Zickermann, High-resolution cryo-EM structures of respiratory complex I: mechanism, assembly, and disease, Sci. Adv. 5 (12) (2019) eaax9484.
[67] R. Guo, S. Zong, M. Wu, J. Gu, M. Yang, Architecture of human mitochondrial respiratory Megacomplex I(2)III(2)IV(2), Cell 170 (6) (2017) 1247–1257 e12.
[68] J. Schiller, E. Laube, I. Wittig, W. Kuhlbrandt, J. Vonck, V. Zickermann, Insights into complex I assembly: function of NDUFAF1 and a link with cardiolipin remodeling, Sci. Adv. 8 (46) (2022) eadd3855.
[69] G. van Meer, D.R. Voelker, G.W. Feigenson, Membrane lipids: where they are and how they behave, Nat. Rev. Mol. Cell Biol. 9 (2) (2008) 112–124.
[70] D.M. van Aalten, A. Amadei, A.B. Linssen, V.G. Eijsink, G. Vriend, H.J. Berendsen, The essential dynamics of thermolysin: confirmation of the hinge-bending motion and comparison of simulations in vacuum and water, Proteins 22 (1) (1995) 45–54.
[71] J. Palma, G. Pierdominici-Sottile, On the uses of PCA to characterise molecular dynamics simulations of biological macromolecules: basics and tips for an effective use, Chemphyschem 24 (2) (2023) e202200491.
[72] Y. Mu, P.H. Nguyen, G. Stock, Energy landscape of a small peptide revealed by dihedral angle principal component analysis, Proteins 58 (1) (2005) 45–52.
[73] V. Carelli, A. Ghelli, L. Bucchi, P. Montagna, A. De Negri, V. Leuzzi, C. Carducci, G. Lenaz, E. Lugaresi, M. Degli Esposti, Biochemical features of mtDNA 14484 (ND6/M64V) point mutation associated with Leber's hereditary optic neuropathy, Ann. Neurol. 45 (3) (1999) 320–328.
[74] E. Ruiz-Pesini, M.T. Lott, V. Procaccio, J.C. Poole, M.C. Brandon, D. Mishmar, C. Yi, J. Kreuziger, P. Baldi, D.C. Wallace, An enhanced MITOMAP with a global mtDNA mutational phylogeny, Nucleic Acids Res. 35 (Database issue) (2007) D823–D828.
[75] K.H. Lee, D.R. Benson, K. Kuczera, Transitions from alpha to pi helix observed in molecular dynamics simulations of synthetic peptides, Biochemistry 39 (45) (2000) 13737–13747.
[76] B. Webb, A. Sali, Comparative protein structure modeling using MODELLER, Curr. Protoc. Bioinformatics 54 (2016) 5.6.1–5.6.37.
[77] E.F. Pettersen, T.D. Goddard, C.C. Huang, G.S. Couch, D.M. Greenblatt, E.C. Meng, T.E. Ferrin, UCSF Chimera–a visualization system for exploratory research and analysis, J. Comput. Chem. 25(13) (2004) 1605–12.
[78] Y. Qi, H.I. Ingolfsson, X. Cheng, J. Lee, S.J. Marrink, W. Im, CHARMM-GUI Martini maker for coarse-grained simulations with the Martini force field, J Chem Theory Comput 11 (9) (2015) 4486–4494.
[79] P.C. Hsu, B.M.H. Bruininks, D. Jefferies, P. Cesar Telles de Souza, J. Lee, D.S. Patel, S.J. Marrink, Y. Qi, S. Khalid, W. Im, CHARMM-GUI Martini maker for modeling and simulation of complex bacterial membranes with lipopolysaccharides, J. Comput. Chem. 38 (27) (2017) 2354–2363.
[80] S. Jo, T. Kim, V.G. Iyer, W. Im, CHARMM-GUI: a web-based graphical user interface for CHARMM, J. Comput. Chem. 29 (11) (2008) 1859–1865.
[81] M.A. Lomize, I.D. Pogozheva, H. Joo, H.I. Mosberg, A.L. Lomize, OPM database and PPM web server: resources for positioning of proteins in membranes, Nucleic Acids Res. 40 (Database issue) (2012) D370–D376.
[82] F.M. Sousa, L.M.P. Lima, C. Arnarez, M.M. Pereira, M.N. Melo, Coarse-grained parameterization of nucleotide cofactors and metabolites: protonation constants, Partition Coefficients, and Model Topologies, J Chem Inf Model 61 (1) (2021) 335–346.
[83] H.J.C. Berendsen, D. van der Spoel, R. van Drunen, GROMACS: a message-passing parallel molecular dynamics implementation, Comput. Phys. Commun. 91 (1) (1995) 43–56.
[84] E. Lindahl, B. Hess, D. van der Spoel, GROMACS 3.0: a package for molecular simulation and trajectory analysis, Molecular modeling annual 7 (8) (2001) 306–317.
[85] D. Van Der Spoel, E. Lindahl, B. Hess, G. Groenhof, A.E. Mark, H.J. Berendsen, GROMACS: fast, flexible, and free, J. Comput. Chem. 26 (16) (2005) 1701–1718.
[86] M. Parrinello, A. Rahman, Polymorphic transitions in single crystals: a new molecular dynamics method, J. Appl. Phys. 52 (12) (1981) 7182–7190.
[87] U. Essmann, L. Perera, M.L. Berkowitz, T. Darden, H. Lee, L.G. Pedersen, A smooth particle mesh Ewald method, J. Chem. Phys. 103 (19) (1995) 8577–8593.
[88] N. Michaud-Agrawal, E.J. Denning, T.B. Woolf, O. Beckstein, MDAnalysis: a toolkit for the analysis of molecular dynamics simulations, J. Comput. Chem. 32 (10) (2011) 2319–2327.
[89] R.T. McGibbon, K.A. Beauchamp, M.P. Harrigan, C. Klein, J.M. Swails, C. X. Hernández, C.R. Schwantes, L.-P. Wang, T.J. Lane, V.S. Pande, MDTraj: a modern open library for the analysis of molecular dynamics trajectories, Biophys. J. 109 (8) (2015) 1528–1532.
[90] G. Pérez-Hernández, S. Tiwari, gph82/Mdciao: First Stable Release Candidate, Zenodo, 2021.
[91] T. Kluyver, B. Ragan-Kelley, F. Pérez, B. Granger, M. Bussonnier, J. Frederic, K. Kelley, J. Hamrick, J. Grout, S. Corlay, P. Ivanov, D. Avila, S. Abdalla, C. Willing, t.

Jupyter development, Jupyter Notebooks ? a publishing format for reproducible computational workflows, in: F. Loizides, B. Scmidt (Eds.) 20th International Conference on Electronic Publishing (01/01/16), IOS Press, pp. 87–90.
[92] J.D. Hunter, Matplotlib: a 2D graphics environment, Computing in Science & Engineering 9 (3) (2007) 90–95.
[93] T.D. Goddard, C.C. Huang, E.C. Meng, E.F. Pettersen, G.S. Couch, J.H. Morris, T. E. Ferrin, U.C.S.F. ChimeraX, Meeting modern challenges in visualization and analysis, Protein Sci. 27 (1) (2018) 14–25.
[94] X. Daura, K. Gademann, B. Jaun, D. Seebach, W.F. van Gunsteren, A.E. Mark, Peptide folding: when simulation meets experiment, Angew. Chem. Int. Ed. 38 (1–2) (1999) 236–240.
[95] L. Rigobello, F. Lugli, L. Caporali, A. Bartocci, J. Fadanni, F. Zerbetto, L. Iommarini, V. Carelli, A.M. Ghelli, M. Francesco, Complex I simulation data.. Zenodo.org, 2023.
[96] S. Kmiecik, D. Gront, M. Kolinski, L. Wieteska, A.E. Dawid, A. Kolinski, Coarse-grained protein models and their applications, Chem. Rev. 116 (14) (2016) 7898–7936.
[97] P.C.T. Souza, R. Alessandri, J. Barnoud, S. Thallmair, I. Faustino, F. Grunewald, I. Patmanidis, H. Abdizadeh, B.M.H. Bruininks, T.A. Wassenaar, P.C. Kroon, J. Melcr, V. Nieto, V. Corradi, H.M. Khan, J. Domanski, M. Javanainen, H. Martinez-Seara, N. Reuter, R.B. Best, I. Vattulainen, L. Monticelli, X. Periole, D. P. Tieleman, A.H. de Vries, S.J. Marrink, Martini 3: a general purpose force field for coarse-grained molecular dynamics, Nat. Methods 18 (4) (2021) 382–388.